Sensorless FOC Strategy for Current Sensor Faults in Three-Phase Induction Motor Drives

A. Gholipour[1], M. Ghanbari[1,], E. Alibeiki[1,2], M. Jannati[1]*

[1]Department of Electrical Engineering, Gorgan Branch, Islamic Azad University, Gorgan, Iran
[2]Department of Electrical Engineering, Aliabad Katoul Branch, Islamic Azad University, Aliabad Katoul, Iran

Abstract- *Current sensors are required in Field-Oriented Control (FOC) strategies of Three-Phase Induction Motor (TPIM) drives. Nevertheless, the current sensors are subject to different electrical/mechanical faults which reduce the safety and dependability of the drive system. Single phase current sensor Fault-Tolerant Control (FTC) for sensorless TPIM drives using flux observer and Extended Kalman Filter (EKF) is proposed in this research. In the suggested FTC scheme, current sensor fault detection is based on axes transformation, a logic circuit is served as the fault isolation and reconstruction of faulted currents are achieved through flux observer and EKF. The presented FTC system is capable of detecting and localizing the current sensor fault and switching the drive system to tolerant FOC mode without the rotor speed measurement. The effectiveness of the suggested FTC system is confirmed by experiments on a 0.75kW TPIM drive platform.*

Keyword: *Current Sensor Fault, EKF, Flux Observer, Sensorless Control, Induction Motor*

NOMENCLATURE

CS	Current sensor
FOC	Field-oriented control
RFOC	Rotor field-oriented control
SFOC	Stator field-oriented control
TPIM	Three-phase induction motor
FTC	Fault-tolerant control
EKF	Extended Kalman filter
FD	Fault detection
FI	Fault isolation
PFC	Post-fault control
ANN	Artificial neural network
FL	Fuzzy logic

1. INTRODUCTION

TPIM drives have been widely used in many industries due to their simple construction, low price, and high efficiency [1-3]. Sensorless control strategies (control strategies without speed sensor) of TPIM drives are known as low cost and high reliable control systems among researchers [4-10]. Sensorless control strategies for TPIM drives can be divided into two main categories: 1) model-based methods which are more suitable for estimation of the TPIM speed in middle and high speed ranges [4-7] and 2) signal-based methods which are more suitable for estimation of the TPIM speed in low speed ranges [8-10].

FOC strategy is one of the powerful control techniques for TPIM drives [2,4,6,8]. This method based on the orientation of the flux is classified as RFOC and SFOC. In RFOC method, the motor flux is aligned with d-axis. Based on this assumption, the stator d-axis current indicates the rotor flux and the stator q-axis current indicates the electromagnetic torque. It means that the TPIM control can be simplified to an easy control system like separately excited DC motor. Normally, FOC strategies for TPIM drives need one inverter, speed sensor, and CSs. Sensors in TPIM drive systems are exposed to some electrical/mechanical failures. Failure of CSs reduces the performance of the TPIM drive system due to the fact that flux position cannot be calculated properly [11].

In some industrial applications particularly in electric vehicles, medical devices, and aerospace, TPIM drive systems are needed to continue their operation even during fault situation. FTC systems have been received great attention due to their ability of increasing the dependability and safety of industrial systems [12-21]. In Ref. [13], a global FTC strategy for FOC of TPIM

drives against the stator winding fault, sensor faults, and broken bars fault was presented. The FD method in Ref. [13] was based on the sliding mode and current spectral analysis. In Ref. [14], two active FTC approaches under speed sensor faults for TPIM drives in electric vehicle powertrains were proposed and compared. The first approach was based on hybrid FTC with PI and H_∞ and the second approach was based on the generalized internal model. For both techniques, the FD was based on the EKF. The presented methods in Ref. [14] were only verified by simulations. In Ref. [15], a passive FTC energy management based on H_∞ for electrical vehicle systems under the DC voltage sensor fault was proposed. Despite the simple construction of passive FTC systems, these methods have less FTC capabilities. In Ref. [18], an active FTC system was developed for FOC of TPIM drives against the stator winding fault. The proposed scheme in Ref. [18] can be used during normal and stator winding fault conditions by only changes in the control parameters. In Ref. [21], two robust FTC techniques for TPIM drives during the IGBT open-circuit fault were proposed. The FD technique in Ref. [21] was based on the Park vector and polar coordinate. The first method was based on the FOC with H_∞ and the second approach was based on the FOC using the conventional inverter with redundant leg.

Commonly, research activities on FTC systems include FD techniques and PFC strategies. In the next subsection, FD and PFC strategies for electric motor drives against CS fault are presented. FD techniques for CSs have been reviewed in many studies. One of the simplest methods for FD is based on the Kirchhoff's law. This fault can be identified if the amount of three actual currents turns to be a nonzero value. This technique needs three CSs to obtain the values of currents. Nevertheless, many TPIM drives utilize only two CSs, and this FD technique cannot be applied. The use of observers is an effective technique for FD. Using this technique, both FD and reconstruction of the faulted current for the FTC system can be performed. However, this method suffers from high complexity due to two observers. In Refs. [22,23], ANN and in Ref. [24], FL methods for FD have been proposed. However, these methods require prior data and large volume of historic information. In Ref. [25], the asymmetry between TPIM currents is utilized for FD in TPIM drives. This strategy is based on the intrinsic features of FOC strategy for TPIM drives and it is not useful for other control schemes such as Direct Torque Control (DTC). In Ref. [26], a FD technique based on axes transformation for TPIM drives was proposed. This method is realized by

comparison of the reference stator currents and the actual stator currents. The proposed strategy in Ref. [26] provides fast and efficient FD.

After FD, there are two possibilities for PFC. In the first method, the control system is switched from a closed-loop system to an open-loop system [27] or to a closed-loop system without current feedback [28]. This method degrades the performance of the drive system noticeably and it is not appropriate for many industries. In the second method, an observer or an additional CS is used to obtain the faulted current value. In this method, a modified closed-loop control system can be used for both pre-fault and post-fault operations. Different strategies based on the second method have been proposed in literature which can be summarized as follows: In Ref. [11], three independent current observers were used for PFC of TPIM drives under CS fault. However, this method suffers from high complexity. In Ref. [26], an observer according to the vector rotator concept was designed to reconstruct the TPIM currents for PFC. In Ref. [26], the reconstructed TPIM currents were obtained based on the real and reference currents. Consequently, the reconstructed currents vary slower than the real currents in transient state. In Ref. [29], a flux-linkage observer was employed for DTC of TPIM drives against CS fault. Nevertheless, this technique requires additional DC-link voltage sensor. Furthermore, the DTC strategy used in Ref. [29] has some problems such as variable switching frequency and high torque ripples especially during low speed operation. In Ref. [30], the reconstruction of the faulted stator current was obtained using the DC-link sensor and switching table. Nevertheless, this technique needs additional DC-link sensor. In Ref. [31], an EKF was used for FOC of TPIM drive systems under sensor faults. However, this method requires position sensor. In Ref. [32], a sliding mode observer with current space vector error projection was employed for sensorless control of synchronous motor drives. In Ref. [33], a control strategy based on the FOC was presented for the CS fault in synchronous motor drives. The proposed technique in Ref. [33] only needs the information of motor currents and rotor position.

Although many control schemes have been proposed for FTC of TPIM drives under CS fault, almost none of the existing schemes could be used for the CS fault in sensorless TPIM drives. In this research, a FTC system using flux observer and EKF is proposed for sensorless TPIM drives. In the suggested FTC scheme, the detection of the fault is done by axes transformation. When the sensor fault is recognized, the process of the

TPIM current estimation becomes active. Flux observer based TPIM model in cooperation with EKF are used to estimate the stator currents. A LC is designed to select the correct current signals. The main contributions of this paper are as follows:

- A FTC strategy is suggested for TPIM drives under CS fault using flux observer and EKF.
- A technique is suggested for FTC of TPIM drives against single phase CS fault without speed measurement.
- A developed RFOC scheme can be shared for healthy and faulty TPIM drive systems.

This research is divided into five Sections. After introduction in Section 1, Section 2 presents the mathematical model of a TPIM. The suggested FTC algorithm is discussed in Section 3. This section includes the influence of the CS fault in sensorless RFOC strategy of a TPIM drive, the structure of the introduced FTC system, the FD technique based on axes transformation, the FI algorithm, and reconstruction of the faulted current using flux observer and EKF. The experimental results are given in Section 4. The last Section is the conclusion.

2. MODEL OF A TPIM

A TPIM is modeled using the following equations [4]:

Stator voltage equation:

$$\begin{bmatrix} v_{ds}^s \\ v_{qs}^s \end{bmatrix} = \begin{bmatrix} r_s + l_s p & 0 \\ 0 & r_s + l_s p \end{bmatrix} \begin{bmatrix} i_{ds}^s \\ i_{qs}^s \end{bmatrix} + \begin{bmatrix} l_m p & 0 \\ 0 & l_m p \end{bmatrix} \begin{bmatrix} i_{dr}^s \\ i_{qr}^s \end{bmatrix} \quad (1)$$

Rotor voltage equation:

$$\begin{bmatrix} v_{dr}^s \\ v_{qr}^s \end{bmatrix} = \begin{bmatrix} 0 \\ 0 \end{bmatrix} = \begin{bmatrix} r_r + l_r p & \Omega_r l_r \\ -\Omega_r l_r & r_r + l_r p \end{bmatrix} \begin{bmatrix} i_{dr}^s \\ i_{qr}^s \end{bmatrix} + \begin{bmatrix} l_m p & \Omega_r l_m \\ -\Omega_r l_m & l_m p \end{bmatrix} \begin{bmatrix} i_{ds}^s \\ i_{qs}^s \end{bmatrix} \quad (2)$$

Stator flux equation:

$$\begin{bmatrix} \varphi_{ds}^s \\ \varphi_{qs}^s \end{bmatrix} = \begin{bmatrix} l_s & 0 \\ 0 & l_s \end{bmatrix} \begin{bmatrix} i_{ds}^s \\ i_{qs}^s \end{bmatrix} + \begin{bmatrix} l_m & 0 \\ 0 & l_m \end{bmatrix} \begin{bmatrix} i_{dr}^s \\ i_{qr}^s \end{bmatrix} \quad (3)$$

Rotor flux equation:

$$\begin{bmatrix} \varphi_{dr}^s \\ \varphi_{qr}^s \end{bmatrix} = \begin{bmatrix} l_m & 0 \\ 0 & l_m \end{bmatrix} \begin{bmatrix} i_{ds}^s \\ i_{qs}^s \end{bmatrix} + \begin{bmatrix} l_r & 0 \\ 0 & l_r \end{bmatrix} \begin{bmatrix} i_{dr}^s \\ i_{qr}^s \end{bmatrix} \quad (4)$$

Torque equation:

$$\tau_e = n_p \left(l_m i_{qs}^s i_{dr}^s - l_m i_{ds}^s i_{qr}^s \right) \quad (5)$$

Mechanical equation:

$$\tau_e - \tau_l = \frac{1}{n_p} \left(J p \Omega_r + B \Omega_r \right) \quad (6)$$
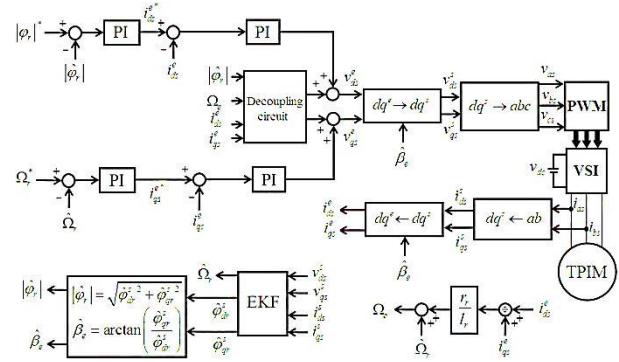

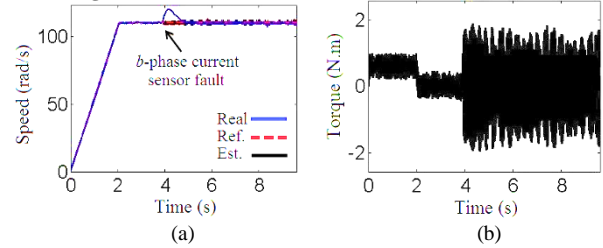
Fig. 1. Basic EKF-based RFOC strategy for a TPIM

Fig. 2. Simulation results of single phase CS fault in basic EKF-based RFOC strategy; (a) speed response, (b) torque response

where, superscript "s" indicates the stationary reference frame. In Refs. (1)-(6), $v_{ds,\,qs}^s$ and $v_{dr,\,qr}^s$ are TPIM voltages. $\varphi_{ds,\,qs}^s$ and $\varphi_{dr,\,qr}^s$ are the TPIM fluxes. $i_{ds,\,qs}^s$ and $i_{dr,\,qr}^s$ are the TPIM currents. $r_{s,\,r}$ are the resistances. $l_{s,\,r,\,m}$ are the self and mutual inductances ($l_s = l_{ls} + l_m$ and $l_r = l_{lr} + l_m$). l_{ls}, l_r are the leakage inductances. $\tau_{e,\,l}$ are the TPIM torque and load torque. Ω_r is the rotor electrical speed. $P = d/dt$. n_p, J, B are the number of pole pairs, moment of inertia and viscous friction coefficient.

3. PROPOSED FTC ALGORITHM

3.1. Influence of the CS fault in sensorless RFOC strategy of a TPIM drive

In this section, the influence of the CS fault in sensorless RFOC strategy of a TPIM is studied with some simulations. For this end, a sensorless TPIM drive system with the basic EKF-based RFOC strategy based on [4], is modelled for simulations. The basic EKF-based RFOC strategy for a TPIM is illustrated in Fig. 1.

Fig. 2 displays Matlab simulation results of single phase CS fault in the basic EKF-based RFOC strategy. In Fig. 2, the TPIM flux is set to 1wb. In addition, the b-phase CS output is made "0" at t=3.88s. The parameters and rated values of the TPIM are given in Appendix. As shown, once the CS fails, speed and torque signals react to this fault during both transient and steady-states. It is seen that after the CS fault, high speed and torque ripples appear in the speed and torque responses. It means that the basic EKF-based RFOC strategy is unable to control the drive system during the CS fault suitably.
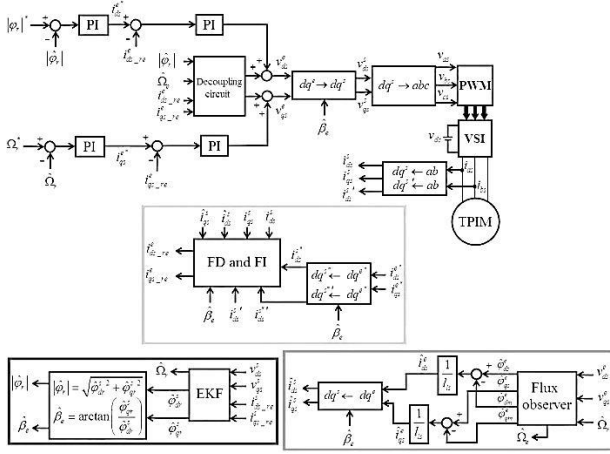
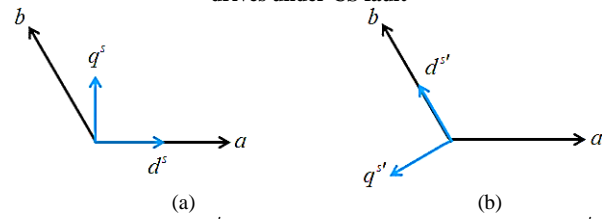**Fig. 3. Structure of the suggested FTC system for sensorless TPIM drives under CS fault**

(a)   (b)

Fig. 4. ab, dq^s, and $dq^{s'}$ axes; (a) d^s-axis aligns with a-axis, (b) $d^{s'}$-axis aligns with b-axis
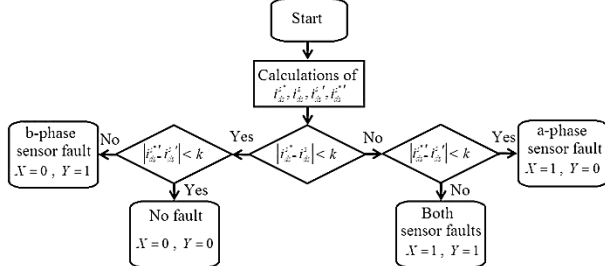

Fig. 5. Flow chart of FD mechanism based on axes transformation

3.2. Structure of the suggested FTC system

The structure of the suggested FTC for sensorless TPIM drives under CS fault is exposed in Fig. 3.

In Fig. 3:

$$\begin{bmatrix} i_{ds}^{s*} \\ i_{qs}^{s*} \end{bmatrix} = \begin{bmatrix} \cos\beta_e & -\sin\beta_e \\ \sin\beta_e & \cos\beta_e \end{bmatrix} \begin{bmatrix} i_{ds}^{e*} \\ i_{qs}^{e*} \end{bmatrix} \tag{7}$$

$$\begin{bmatrix} i_{ds}^{s*'} \\ i_{qs}^{s*'} \end{bmatrix} = \begin{bmatrix} \cos\left(\beta_e - \dfrac{2\pi}{3}\right) & -\sin\left(\beta_e - \dfrac{2\pi}{3}\right) \\ \sin\left(\beta_e - \dfrac{2\pi}{3}\right) & \cos\left(\beta_e - \dfrac{2\pi}{3}\right) \end{bmatrix} \begin{bmatrix} i_{ds}^{e*} \\ i_{qs}^{e*} \end{bmatrix} \tag{8}$$

In Eqns. (7) and (8), superscript "e" and "$*$" indicate the rotational reference frame and reference value, respectively. In addition, β_e is the rotor flux angle.

Generally, this system includes a RFOC strategy, FD and FI algorithms, flux observer, and EKF. Based on Fig. 3, the estimated values of the TPIM currents are obtained using the flux observer and some simple calculations. The EKF is considered for the estimation

of the rotor flux and TPIM speed. The estimated values of the rotor flux angle and rotor speed are applied to the flux observer. In the suggested scheme after FD of the CS, the FI algorithm which is based on the LC selects the right current signals to continue the operation of the TPIM drive. In Fig. 3, during healthy condition the actual TPIM currents are used for the RFOC system. In this condition, the system operates as the basic EKF-based RFOC strategy. When the fault occurs, the corresponding estimated values of the stator currents are used for the RFOC system.

3.3. FD technique based on axes transformation

This section presents the FD mechanism based on axes transformation. It is assumed that two CSs are employed to measure stator a-phase and b-phase currents. ab, dq^s, and $dq^{s'}$ axes can be illustrated as Fig. 4. In Fig. 4(a) it is assumed that the d^s-axis aligns with a-axis and in Fig. 4(b) it is assumed that the $d^{s'}$-axis aligns with b-axis.

Based on Fig. 4(a), the transformation matrix to transform the TPIM currents from ab frame to dq^s frame is as Eq. (9). In addition, based on Fig. 4(b), the transformation matrix to transform the TPIM currents from ab frame to $dq^{s'}$ frame is as (10).

$$\begin{bmatrix} i_{ds}^{s} \\ i_{qs}^{s} \end{bmatrix} = \begin{bmatrix} 1 & 0 \\ \dfrac{\sqrt{3}}{3} & \dfrac{2\sqrt{3}}{3} \end{bmatrix} \begin{bmatrix} i_{as} \\ i_{bs} \end{bmatrix} \tag{9}$$

$$\begin{bmatrix} i_{ds}^{s\,'} \\ i_{qs}^{s\,'} \end{bmatrix} = \begin{bmatrix} 0 & 1 \\ -\dfrac{2\sqrt{3}}{3} & -\dfrac{\sqrt{3}}{3} \end{bmatrix} \begin{bmatrix} i_{as} \\ i_{bs} \end{bmatrix} \tag{10}$$

As can be seen from Eq. (9), the stator d^s-axis current is independent of the stator b-axis current. Moreover, from Eq. (10) it is observed that the stator $d^{s'}$-axis current is independent of the stator a-axis current. Based on Eq. (9), when the CS fault happens in a-axis, the value of i_{ds}^s is incorrect. In this condition, $|i_{ds}^{s*} - i_{ds}^s| > k$. In addition, based on (10), the value of $i_{ds}^{s'}$ is correct. It means $|i_{ds}^{s*'} - i_{ds}^{s'}| < k$. According to this, the flow chart of the FD mechanism based on axes transformation is shown in Fig. 5. As shown, the FD can be realized by comparison between the actual stator currents based on Eqns. (9), (10) and the reference stator currents (i_{ds}^{s*}, $i_{ds}^{s*'}$). It is worth mentioning that the reference stator currents can be obtained from RFOC system as shown in Fig. 3.

In Fig. 5, k is the threshold value. During normal condition when both CSs are healthy and the TPIM operates under sensorless control strategy, the current residual signal is smaller than the threshold value. When fault happens, the current residual signal amplitude is

larger than the threshold value and therefore the fault can be detected. Based on Fig. 5, the values of X and Y are selected after FD. Based on X and Y values, the actual or estimated stator currents based on the FI algorithm are chosen. The actual or estimated stator currents are then used as feedback signals.

3.4. FI algorithm
Fig. 6 illustrates the LC for the FI. In this figure, two switches are considered. When the input of S_1 (red color in Fig. 6) is "0", the switch is in position "0", while when the input of S_1 is "1", the switch is in position "1". Additionally, when the input of S_2 (blue color in Fig. 6) is "0", the switch is in position "0", while when the input of S_2 is "1", the switch is in position "1".

As can be observed from Fig. 5, when b-phase CS fails the values of X and Y are "0" and "1", respectively. In this case, based on Fig. 6, the actual value of the stator d-axis current and the estimated value of the stator q-axis current are selected. In addition, when a-phase CS fails the values of X and Y are "1" and "0", respectively. In this case, the estimated values of the stator dq^s currents are selected. Furthermore, during normal mode, the values of X and Y are "0" and "0", respectively. In this case, the actual values of the stator dq^s currents are selected. It should be mentioned that the CS fault do not essentially mean an open-circuit fault, any malfunctions in CS can be considered as CS fault.

3.5. Reconstruction of the faulted current using flux observer and EKF
When the CS fault occurs, the drive system should switch to the FTC system. In this condition, the TPIM currents require to be reconstructed. This section presents the suggested technique for estimation of the TPIM currents. The mutual fluxes ($\varphi^e_{dm,\ qm}$) and stator fluxes ($\varphi^e_{ds,\ qs}$) can be estimated as (11) and (12), respectively:

$$\begin{bmatrix} \hat{\varphi}^e_{dm} \\ \hat{\varphi}^e_{qm} \end{bmatrix} = \begin{bmatrix} \dfrac{l_{m1}}{l_{ls}} & 0 & \dfrac{l_{m1}}{l_{lr}} & 0 \\ 0 & \dfrac{l_{m1}}{l_{ls}} & 0 & \dfrac{l_{m1}}{l_{lr}} \end{bmatrix} \begin{bmatrix} \hat{\varphi}^e_{ds} \\ \hat{\varphi}^e_{qs} \\ \varphi^e_{dr} \\ \varphi^e_{qr} \end{bmatrix} \quad (11)$$

$$\begin{bmatrix} p\hat{\varphi}^e_{ds} \\ p\hat{\varphi}^e_{qs} \end{bmatrix} = \begin{bmatrix} -\dfrac{r_s}{l_{ls}} & \hat{\Omega}_e & \dfrac{r_s}{l_{ls}} & 0 \\ -\hat{\Omega}_e & -\dfrac{r_s}{l_{ls}} & 0 & \dfrac{r_s}{l_{ls}} \end{bmatrix} \begin{bmatrix} \hat{\varphi}^e_{ds} \\ \hat{\varphi}^e_{qs} \\ \hat{\varphi}^e_{dm} \\ \hat{\varphi}^e_{qm} \end{bmatrix} + \begin{bmatrix} v^e_{ds} \\ v^e_{qs} \end{bmatrix} \quad (12)$$

where, superscript "^" indicates the estimated value. Furthermore,

$$l_{m1} = \frac{l_m l_{ls} l_{lr}}{l_{ls} l_{lr} + l_m l_{lr} + l_m l_{ls}} \quad (13)$$

$$\hat{\Omega}_e = \hat{\Omega}_r + \frac{\hat{\varphi}^e_{ds} \hat{i}^e_{qs} - \hat{\varphi}^e_{qs} \hat{i}^e_{ds}}{2\left(\hat{\varphi}^e_{dm}{}^2 + \hat{\varphi}^e_{qm}{}^2\right)} r_r \quad (14)$$

In Eq. (14), $\hat{\Omega}_e$ is the estimated rotor angular speed. Based on RFOC principle, the values of the rotor fluxes used in Eq. (11) can be written as Eqns. (15) and (16):

$$\varphi^e_{dr} = \left|\varphi_r\right|^* \quad (15)$$

$$\varphi^e_{qr} = 0 \quad (16)$$

where, $\left|\varphi_r\right|^*$ is the reference rotor flux amplitude. The stator currents can be written as Eq. (17) [34]:

$$\begin{bmatrix} \hat{i}^e_{ds} \\ \hat{i}^e_{qs} \end{bmatrix} = \begin{bmatrix} \dfrac{1}{l_{ls}} & 0 & -\dfrac{1}{l_{ls}} & 0 \\ 0 & \dfrac{1}{l_{ls}} & 0 & -\dfrac{1}{l_{ls}} \end{bmatrix} \begin{bmatrix} \hat{\varphi}^e_{ds} \\ \hat{\varphi}^e_{qs} \\ \hat{\varphi}^e_{dm} \\ \hat{\varphi}^e_{qm} \end{bmatrix} \quad (17)$$

Consequently, based on Eqns. (11)-(17), the flux observer for estimation of the TPIM currents can be shown in Fig. 7.

As can be seen from Fig. 7, the TPIM speed and rotor flux angle are needed for estimation of the stator currents. In this research, a full order EKF is used to estimate the TPIM speed and rotor flux. The EKF is a model-based stochastic estimator. Compared to other estimation techniques, this algorithm can estimate state components considering system and measurement noises. This technique can estimate the TPIM speed acceptably and the drive system can continue its desired performance under this method.
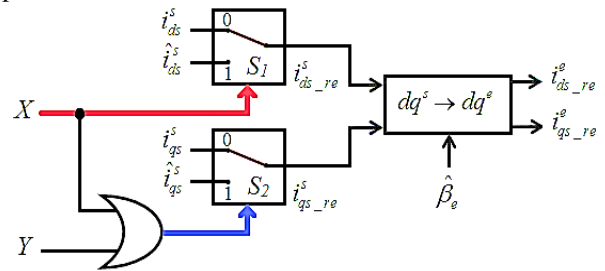

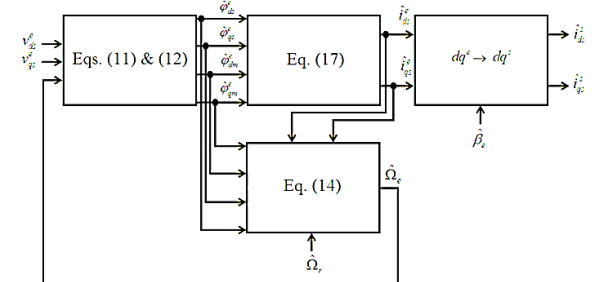
Fig. 6. LC for the FI

Fig. 7. Flux observer for estimation of the TPIM currents

To estimate the TPIM speed and flux using EKF, the TPIM model under taking noise into consideration can be expressed as Eqns. (18) and (19):

$$x_{k+1} = f(x_k) + B_k u_k + v_k \tag{18}$$

$$y_k = H_k x_k + w_k \tag{19}$$

$$x_k = \begin{bmatrix} i_{ds,k}^s \\ i_{qs,k}^s \\ \varphi_{dr,k}^s \\ \varphi_{qr,k}^s \\ \Omega_{r,k} \end{bmatrix}, \; u_k = \begin{bmatrix} v_{ds,k}^s \\ v_{qs,k}^s \end{bmatrix}, \; B_k = \begin{bmatrix} \dfrac{1}{l_\sigma} & 0 \\ 0 & \dfrac{1}{l_\sigma} \\ 0 & 0 \\ 0 & 0 \\ 0 & 0 \end{bmatrix} \tag{20}$$

$$H_k = \begin{bmatrix} 1 & 0 & 0 & 0 & 0 \\ 0 & 1 & 0 & 0 & 0 \end{bmatrix}, \; l_\sigma = l_s - \frac{l_m^2}{l_r}$$

$$f(x_k) = x_k \cdot \begin{bmatrix} 1 - \frac{1}{l_\sigma}\left(r_s + \frac{r_r l_m^2}{l_r^2}\right)T & 0 & \frac{r_r l_m}{l_\sigma l_r^2}T & \frac{\Omega_{r,k} l_m}{l_\sigma l_r}T & 0 \\ 0 & 1 - \frac{1}{l_\sigma}\left(r_s + \frac{r_r l_m^2}{l_r^2}\right)T & -\frac{\Omega_{r,k} l_m}{l_\sigma l_r}T & \frac{r_r l_m}{l_\sigma l_r^2}T & 0 \\ \frac{r_r l_m}{l_r}T & 0 & 1 - \frac{r_r}{l_r}T & -\Omega_{r,k}T & 0 \\ 0 & \frac{r_r l_m}{l_r}T & \Omega_{r,k}T & 1 - \frac{r_r}{l_r}T & 0 \\ 0 & 0 & 0 & 0 & 1 \end{bmatrix}$$

In Eqns. (18)-(20), T is the sampling period. It is worth mentioning that, in Eq. (20) with a very large moment of inertia, $p\Omega_r = 0$. u_k, x_k, and y_k are input, state, and output vectors. v_k and w_k are the system and measurement noises. f is a nonlinear function of inputs and states. B_k and H_k are input and measurement matrices. The recursive EKF algorithm contains three steps as Eqns. (21)-(25) [4]:

Prediction process:

$$\tilde{x}_k = f(\hat{x}_{k-1}) + B_{k-1}u_{k-1} \tag{21}$$

$$\tilde{P}_k = F_k \hat{P}_{k-1} F_k^T + Q_{k-1} \tag{22}$$

Kalman filter gain:

$$K_k = \tilde{P}_k H_k^T \left(H_k \tilde{P}_k H_k^T + R_k\right)^{-1} \tag{23}$$

Filter process:

$$\hat{x}_k = \tilde{x}_k + K_k\left(y_k - H_k \tilde{x}_k\right) \tag{24}$$

$$\hat{P}_k = \left(I - K_k H_k\right)\tilde{P}_k \tag{25}$$

where, P_k, Q_k, and R_k are the state estimation error, system noise, and measurement noise covariance matrices, respectively. The system and measurement noise covariance matrices are defined as Eqns. (26) and (27), respectively.

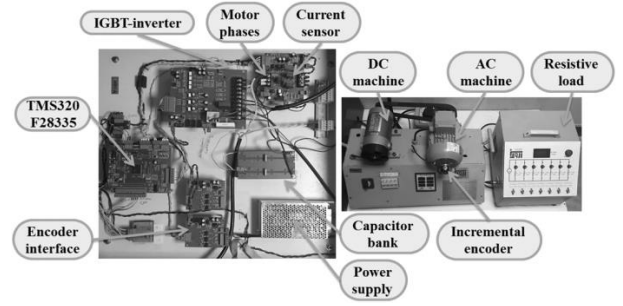$$Q_k = E\begin{bmatrix} v_k & v_k^T \end{bmatrix} \tag{26}$$

Fig. 8. Picture of the experimental set up

$$R_k = E\begin{bmatrix} w_k & w_k^T \end{bmatrix} \tag{27}$$

As can be seen from Eqns. (21)-(25), in the recursive algorithm of EKF instead of v_k and w_k, Q_k and R_k are used. It is worth mentioning that, the matrix Q_k includes model uncertain, process disturbances, inaccuracy of machine, etc. In addition, the matrix R_k includes measurement noises and A/D quantization.

Based on Eqns. (18)-(27), the TPIM speed and dq^s rotor fluxes can be estimated. The rotor flux amplitude and angle can be calculated based on estimated values of dq^s rotor fluxes as Eqns. (28) and (29), respectively:

$$|\hat{\varphi}_r| = \sqrt{\hat{\varphi}_{dr}^{s\,2} + \hat{\varphi}_{qr}^{s\,2}} \tag{28}$$

$$\hat{\beta}_e = \arctan\left(\frac{\hat{\varphi}_{qr}^s}{\hat{\varphi}_{dr}^s}\right) \tag{29}$$

4. EXPERIMENTAL RESULTS

The performance of the introduced FTC strategy for RFOC of a TPIM drive is experimentally confirmed with a DSP/TMS320F28335-based experimental set up. All tests are performed in the operation of sensorless control. The picture of the experimental set up of a 0.75kW four-pole TPIM is shown in Fig. 8.

In tests, the sampling time is 100μs. Furthermore, the TPIM flux is set to 1wb and TPIM torque is calculated based on the RFOC equations ($\tau_e = (n_p l_m |\hat{\varphi}_r| i_{qs\_re}^e)/l_r$). The code of the introduced FTC system for the DSP is generated using PSIM software. The switching frequency of the inverter and the DC-link voltage are 10kHz and 380V, respectively. Diode bridge rectifier-inverter is the foundation of the system used in this paper. This topology is one of the most common types of systems for industrial applications. This topology includes a basic three-phase diode bridge rectifier (which allows energy flow from the power supply to the DC-link), DC-link capacitor, and voltage source inverter. The inverter is built using six IGBT modules. The value of the current residual

signal threshold value is set to 0.4A in tests ($k = 0.4A$). The parameters and rated values of the TPIM in the experiments as well as the control parameters are given in Tables 1 and 2. Some experimental results during different operation conditions are presented here.

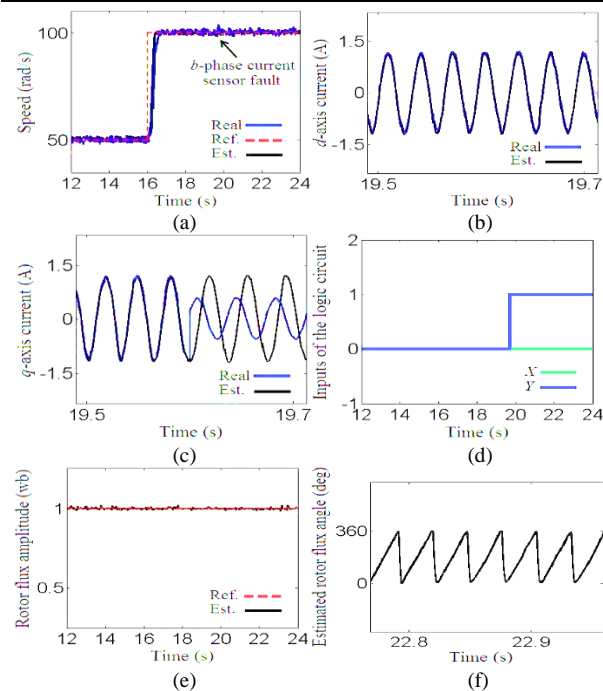### 4.1. FTC of the sensorless TPIM drive during no-load condition when *b*-phase CS fails

The results of the introduced FTC during no-load condition when *b*-phase CS fails are illustrated in Fig. 9. In Fig. 9, the *b*-phase CS output in PSIM software is made "0" at t=19.6s.

Table 1. Parameters and rated values of the TPIM

Parameter	Value
Rating	0.75kW, 380V, 50Hz, 5.1N.m, 148.1rad/s
r_s	10.45Ω
r_r	14.65Ω
l_s, l_r	0.61H
l_m	0.6H
n_p	2
J	0.016kg.m²

Table 2. Control parameters

| Parameter	Value
Speed controller	K_p=1 , K_i=1.2
Current controllers	K_p=82 , K_i=8
Flux controller	K_p=21 , K_i=2
Sampling time	100μs
Reference flux	1wb
k	0.4A

Fig. 9. Experimental results of the sensorless TPIM drive during no-load condition when *b*-phase CS fails; (a) real, reference, and estimated speeds, (b) real and estimated *d*-axis currents; (c) real and estimated *q*-axis currents, (d) inputs of the LC, (e) rotor flux amplitude, (f) estimated rotor flux angle

Fig. 9(a) illustrates the good speed tracking performance during both normal and single phase CS fault conditions. Based on Fig. 9(a), the delay caused by the estimation and measurement process is about 0.2s. Real and estimated dq^s currents are illustrated in Fig.

9(b) and Fig. 9(c). As shown in these figures, the real *d*-axis current in the faulty mode has correct value. However, the real *q*-axis current is affected by the fault and produce incorrect value. As shown in Fig. 5 and Fig. 6, in this condition the real *d*-axis current and the estimated *q*-axis current are used in the control system. Fig. 9(d) shows the inputs of the LC. As can be seen from this figure, before t=19.6s the values of *X* and *Y* are "0" and "0", demonstrating that both sensors are healthy. In addition, after t=19.6s, the values of *X* and *Y* are "0" and "1", representing that *a*-phase CS is healthy and *b*-phase CS is faulty. Fig. 9(e) illustrates the good performance of the rotor flux tracking. Fig. 9(f) displays the good performance of the EKF for estimation of the rotor flux angle during the fault. The results of Fig. 9 show good performances of the FD and FI mechanisms, flux observer, and EKF estimator when *b*-phase CS fails.

### 4.2. FTC of the sensorless TPIM drive during no-load condition when *a*-phase CS fails

The results of the suggested FTC method during no-load condition when *a*-phase CS fails are illustrated in Fig. 10. In Fig. 10, the *a*-phase CS output is made "0" at t=19.6s. The real, reference, and estimated speeds of the TPIM drive under such condition are illustrated in Fig. 10(a). This figure depicts the satisfactory operation of the introduced FTC scheme in the occurrence of *a*-phase CS fault.
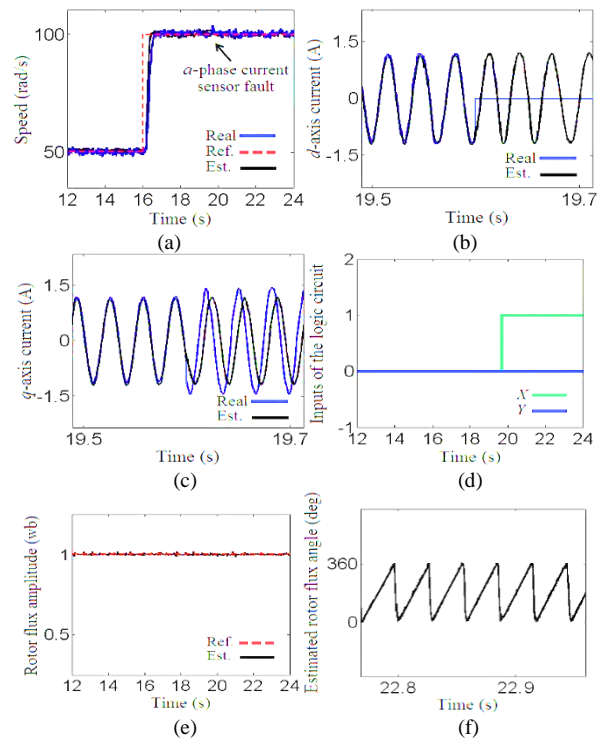
Fig. 10. Experimental results of the sensorless TPIM drive during no-load condition when *a*-phase CS fails; (a) real, reference, and estimated speeds, (b) real and estimated *d*-axis currents; (c) real and estimated *q*-axis currents, (d) inputs of the LC, (e) rotor flux amplitude, (f) estimated rotor flux angle
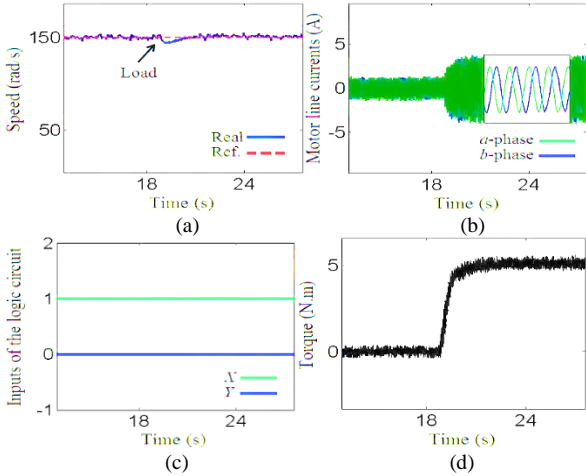
Fig. 11. Experimental results of the post-fault operation of the suggested FTC system for sensorless TPIM drive under load condition when *a*-phase CS fails; (a) real and reference speeds, (b) TPIM line currents, (c) inputs of the LC, (d) torque
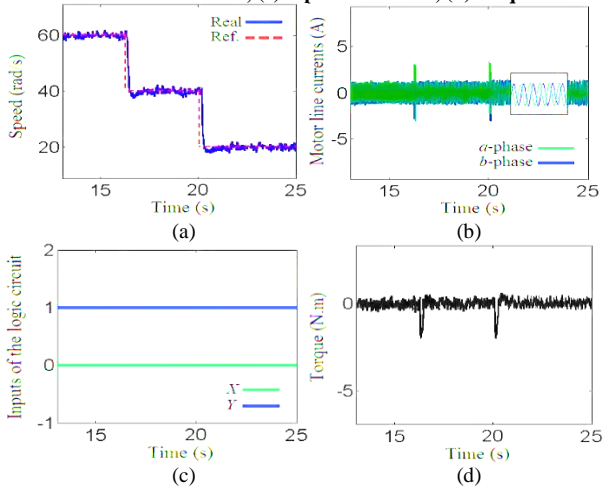
Fig. 12. Experimental results of the post-fault operation of the suggested FTC system during different speeds when *b*-phase CS fails; (a) real and reference speeds, (b) TPIM line currents, (c) inputs of the LC, (d) torque

Based on Fig. 10(a), the delay caused by the estimation and measurement process is about 0.15s. Fig. 10(b) and Fig. 10(c) show the real and estimated dq^s stator currents under healthy and faulty conditions. Under such a condition, both real dq^s currents are affected and generate incorrect values. In this condition, the real dq^s currents are replaced by the estimated dq^s currents. Fig. 10(d) shows the status of X and Y. Under normal condition, the values of X and Y are "0" and "0". Nevertheless, during faulty condition the values of X and Y change to "1" and "0", demonstrating that *a*-phase CS fails. The estimated rotor flux amplitude is represented in Fig. 10(e), which shows a constant flux operation even under the faulty condition. Fig. 10(f) shows the suitable performance of the EKF algorithm for estimation of the rotor flux angle after *a*-phase CS fault. From the experimental results of Fig. 10, it can be observed that the drive system can successfully switch from the sensorless RFOC method to the suggested

sensorless FTC system when *a*-phase CS fails.

4.3. Post-fault operation of the suggested FTC system for sensorless TPIM drive under load condition when *a*-phase CS fails

The experimental results of the post-fault operation of the sensorless TPIM drive under load condition when *a*-phase CS fails are shown in Fig. 11. In this test, a DC generator which is driven by a resistive load unit is mechanically coupled to the TPIM to generate the load torque. In this scenario, at t=19.93s, a load torque equal to 5.1N.m (rated torque) is introduced. Fig. 11(a) shows good speed tracking performance under no-load and load conditions. The TPIM line currents are shown in Fig. 11(b), demonstrating that the currents are perfectly sinusoidal and balanced. Fig. 11(c) shows X=1 and Y=0, demonstrating that *a*-phase CS is faulty and *b*-phase CS is healthy. Fig. 11(d) shows the TPIM torque during the faulty mode. As can be seen from Fig. 11(d), the TPIM torque has reasonable ripples and its average value, except during transient state, under no-load condition is equal to zero and under load condition is the same as the applied mechanical load. Fig. 11 shows that the suggested FTC system for sensorless TPIM drive provides stable operation even during load condition.
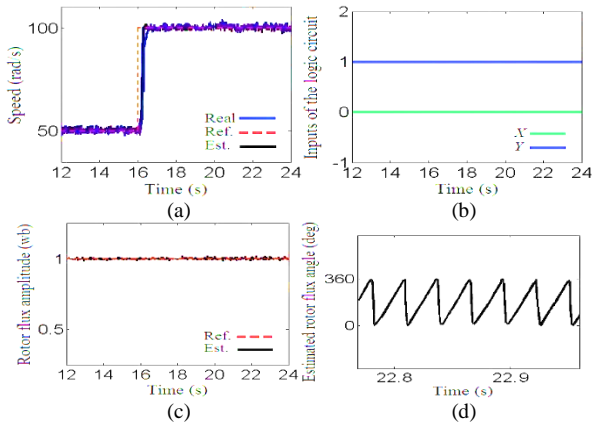
4.4. Post-fault operation of the suggested FTC system for sensorless TPIM drive during different speeds when *b*-phase CS fails

The experimental results of the post-fault operation of the sensorless TPIM drive during different speeds when *b*-phase CS fails are illustrated in Fig. 12. In this scenario, the reference TPIM speed is set to 60rad/s, 40rad/s, and 20rad/s. Fig. 12(a) shows the real speed can track its reference value during different speeds. As can be seen from Fig. 12(b) the TPIM line currents are sinusoidal and balanced. Fig. 12(c) indicates that the good performance of the FD mechanism. Fig. 12(d) displays the acceptable TPIM torque during different speeds. As can be observed from Fig. 12(d) the TPIM torque average value except during transient state is equal to zero because of the no-load condition.

4.5. Post-fault operation of the suggested FTC system during different speeds when *a*-phase CS fails

Fig. 13 illustrates the experimental results of the introduced FTC system after the fault during different speeds and no-load condition when *a*-phase CS fails. In Fig. 13, the *a*-phase CS output in PSIM software is made "0". It can be observed that the CS fault has almost negligible influence on the performance of the drive system as the experimental results of Fig. 13 are similar to the experimental results of the healthy TPIM drive as depicted in Fig. 9.
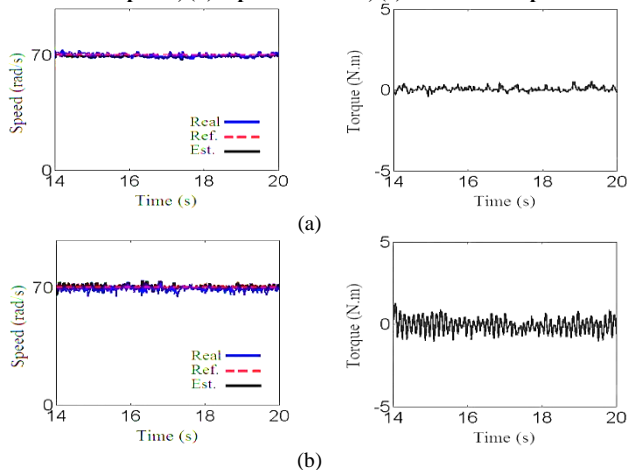
Fig. 13. Experimental results of the sensorless TPIM drive during different speeds when *a*-phase CS fails; (a) real, reference, and estimated speeds, (b) inputs of the LC, (c) rotor flux amplitude, (d) estimated rotor flux angle
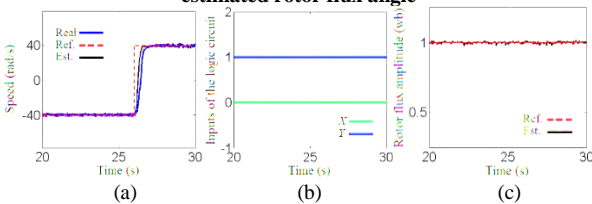
Fig. 14. Experimental results of the post-fault operation of sensorless TPIM drive while the reference speed changes from -40rad/s to +40rad/s when *b*-phase CS fails; (a) real, reference, and estimated speeds, (b) inputs of the LC, (c) rotor flux amplitude

Fig. 15. Experimental results of the post-fault operation of the suggested FTC system and the post-fault operation of the basic EKF-based RFOC strategy when *b*-phase CS fails; (a) suggested FTC system, (b) basic EKF-based RFOC strategy

4.6. Post-fault operation of the suggested FTC system for sensorless TPIM drive while the reference speed changes from -40rad/s to +40rad/s when *b*-phase CS fails

The experimental results of the post-fault operation of the suggested FTC system for sensorless TPIM drive while the reference speed changes from -40rad/s to +40rad/s when *b*-phase CS fails are shown in Fig. 14. Fig. 14(a) shows real and estimated speeds can follow the reference speed. Additionally, the real rotor flux can track the reference rotor flux during different speeds. Fig. 14(b) specifies that the good performance of the presented FD system.

4.7. Post-fault operation of the suggested FTC system and the post-fault operation of the basic EKF-based RFOC strategy when *b*-phase CS fails

The experimental results of the post-fault operation of the suggested FTC system based on Fig. 3 and the post-fault operation of the basic EKF-based RFOC strategy based on Fig. 1 when *b*-phase CS fails are shown in Fig. 15. As can be observed the basic EKF-based RFOC strategy is unable to control the sensorless TPIM drive during the CS fault appropriately. As shown, during the post-fault operation, the speed and torque oscillations of the basic EKF-based RFOC strategy are very high when compared to the speed and torque oscillations of the suggested FTC system. From the experimental results of Figs. 9-15, it can be observed that the suggested FTC algorithm could serve as a backup control system in the case of single phase CS fault for sensorless TPIM drives. The suggested FTC system guarantees the good performance of the sensorless drive system during different situations.

5. CONCLUSION

To improve the reliability of TPIM drive systems, this research has presented a sensorless RFOC technique for FTC of TPIM drives under CS fault based on flux observer and EKF. In the suggested scheme, the FD is based on axes transformation. The LC is used as the FI algorithm and flux observer in cooperation with EKF are utilized for reconstruction of the faulted currents and TPIM speed estimation. The suggested strategy can rapidly realize the FD of the CS and switch to the corresponding FTC system quickly. The experimental results on a 0.75kW TPIM drive platform confirm the satisfactory working of the introduced FTC strategy during different operation conditions. The results indicate that presented scheme is a good choice for FTC of sensorless TPIM drive systems under CS fault. The proposed strategy in this research runs for a sensorless RFOC of TPIM drive. However, this method with some modifications could be extended for sensored RFOC of TPIM drives under speed sensor and CS faults.

REFERENCES

[1] H. Moayedirad and S. Nejad, "Increasing the efficiency of the power electronic converter for a proposed dual stator winding squirrel-cage induction motor drive using a five-leg inverter at low speeds", *J. Oper. Autom. Power Eng.*, vol. 6, no. 1, pp. 23-39, 2018.

[2] R. Tabasian et al., "Direct field-oriented control strategy for fault-tolerant control of induction machine drives based on EKF", *IET Electr. Power Appl.*, 2020.

[3] M. Shabandokht-Zarami et al., "An improved FOC strategy for speed control of induction motor drives under an open-phase fault using genetic algorithm", *J. Oper. Autom. Power Eng.*, vol. 10, no. 1, pp. 80-89, 2022.

[4]   M. Nikpayam et al., "Fault-tolerant control of Y-connected three-phase induction motor drives without speed measurement", *Measure.,* vol. 149, pp. 1-14, 2020.

[5]   A. Ammar et al., "Feedback linearization based sensorless direct torque control using stator flux MRAS-sliding mode observer for induction motor drive", *ISA Trans.,* vol. 98, pp. 382-92, 2020.

[6]   M. Jouili et al., "Luenberger state observer for speed sensorless ISFOC induction motor drives", *Electr. Power Syst. Res.,* vol. 89, pp. 139-47, 2012.

[7]   A. Pal and S. Das, "Development of energy efficient scheme for speed sensorless induction motor drive", *Int. Trans. Electr. Energy Syst.,* 2020.

[8]   Z. Zhang et al., "Sensorless direct field-oriented control of three-phase induction motors based on "Sliding Mode" for washing-machine drive applications", *IEEE Trans. Ind. Appl.,* vol. 42, no. 3, pp. 694-701, 2006.

[9]   W. Sun, D. Xu, and D. Jiang, "Observability analysis for speed sensorless induction motor drives with and without virtual voltage injection", *IEEE Trans. Power Electron.,* vol. 34, no. 9, pp. 9236-46, 2018.

[10] J. Holtz, "Sensorless control of induction machines—with or without signal injection?", *IEEE Trans. Ind. Electron.,* vol. 53, no. 1, pp. 7-30, 2006.

[11] M. Hinkkanen, V. Leppanen, and J. Luomi, "Flux observer enhanced with low-frequency signal injection allowing sensorless zero-frequency operation of induction motors", *IEEE Trans. Ind. Appl.,* vol. 41, no. 1, pp. 52-59, 2005.

[12] Y. Yu et al., "Current sensor fault diagnosis and tolerant control for VSI-based induction motor drives", *IEEE Trans. Power Electron.,* vol. 33, pp. 4238-48, 2017.

[13] A. Gouichiche et al., "Global fault-tolerant control approach for vector control of an induction motor", *Int. Trans. Electr. Energy Syst.,* 2020.

[14] A. Raisemche et al., "Two active fault-tolerant control schemes of induction-motor drive in EV or HEV", *IEEE Trans. Veh. Tech.,* vol. 63, no. 1, pp. 19-29, 2013.

[15] R. Oubellil and M. Boukhnifer, "Passive fault tolerant control design of energy management system for electric vehicle", *2014* IEEE 23rd *Int. Symp. Ind. Electron.,* Istanbul, Turkey, 2014.

[16] A. Amin and K. Hasan, "A review of fault tolerant control systems: advancements and applications", *Measure.,* vol. 143, pp. 58-68, 2019.

[17] P. Gangsar and R. Tiwari, "Signal based condition monitoring techniques for fault detection and diagnosis of induction motors: A state-of-the-art review", *Mech. Syst. Signal Proc.,* vol. 144, pp. 1-37, 2020.

[18] M. Jannati et al., "Experimental evaluation of FOC of 3-phase IM under open-phase fault", *Int. J. Electron.,* vol. 104, no. 10, pp. 1675-88, 2017.

[19] D. Zhou et al., "An embedded closed-loop fault-tolerant control scheme for nonredundant vsi-fed induction motor drives", *IEEE Trans. Power Electron.,* vol. 32, no. 5, pp. 3731-40, 2016.

[20] D. Campos-Delgado, D. Espinoza-Trejo, and E. Palacios, "Fault-tolerant control in variable speed drives: a survey", *IET Electr. Power Appl.,* vol. 2, no. 2, pp. 121-34, 2008.

[21] B. Cherif et al., "Indirect vector controlled of an induction motor using H$^{\infty}$ current controller for IGBT open circuit fault compensation", *Int. Trans. Electr. Energy Syst.,* 2020.

[22] A. Bernieri et al., "A neural network approach to instrument fault detection and isolation", *IEEE Trans. Instrument. Measure.,* vol. 44, no. 3, pp. 747-50, 1995.

[23] K. Klimkowski and M. Dybkowski, "Neural network approach for stator current sensor fault detection and isolation for vector controlled induction motor drive", *Int. Power Electron. Motion Control Conf.,* Bulgaria, 2016.

[24] H. Li, A. Monti, and F. Ponci, "A fuzzy-based sensor validation strategy for AC motor drives", *IEEE Trans. Ind. Inf.,* vol. 8, no. 4, pp. 839-48, 2012.

[25] F. Salmasi, "A self-healing induction motor drive with model free sensor tampering and sensor fault detection, isolation, and compensation", *IEEE Trans. Ind. Electron.,* vol. 64, no. 8, pp. 6105-15, 2017.

[26] C. Chakraborty and V. Verma, "Speed and current sensor fault detection and isolation technique for induction motor drive using axes transformation", *IEEE Trans. Ind. Electron.,* vol. 62, no. 3, pp. 1943-54, 2014.

[27] Y. Liu, M. Stettenbenz, and A. Bazzi, "Smooth fault-tolerant control of induction motor drives with sensor failures", *IEEE Trans. Power Electron.,* vol. 34, no. 4, pp. 3544-52, 2018.

[28] B. Tabbache et al., "A control reconfiguration strategy for post-sensor FTC in induction motor-based EVs", *IEEE Trans. Veh. Tech.,* vol. 62, no. 3, pp. 965-71, 2012.

[29] M. Manohar and S. Das, "Current sensor fault-tolerant control for direct torque control of induction motor drive using flux-linkage observer", *IEEE Tran. Ind. Inf.,* vol. 13, no. 6, pp. 2824-33, 2017.

[30] J. Lu et al., "Independent phase current reconstruction strategy for IPMSM sensorless control without using null switching states", *IEEE Trans. Ind. Electron.,* vol. 65, no. 6, pp. 4492-4502, 2017.

[31] X. Zhang et al., "Sensor fault detection, isolation and system reconfiguration based on extended Kalman filter for induction motor drives", *IET Electr. Power Appl.,* vol. 7, no. 7, pp. 607-17, 2013.

[32] G. Zhang et al., "Current sensor fault-tolerant control for encoderless IPMSM drives based on current space vector error reconstruction", *IEEE J. Emerg. Selected Top. Power Electron.,* vol. 8, no. 4, pp. 3658-68, 2019.

[33] C. Wu et al., "A signal-based fault detection and tolerance control method of current sensor for PMSM drive", *IEEE Trans. Ind. Electron.,* vol. 65, no. 12, pp. 9646-57, 2018.

[34] B. Bose, Modern power electronics and AC drives. Prentice hall. 2002.